CYCLONE GLOBAL NAVIGATION SATELLITE SYSTEM (CYGNSS)

Algorithm Theoretical Basis Level 3 Soil Moisture	UM Doc. No.	148-0413
	SwRI Doc. No.	N/A
	Revision	Rev 1
	Date	29 October 2025
	Contract	NNL13AQ00C

Algorithm Theoretical Basis Documents (ATBDs) provide the physical and mathematical descriptions of the algorithms used in the generation of science data products. The ATBDs include a description of variance and uncertainty estimates and considerations of calibration and validation, exception control and diagnostics. Internal and external data flows are also described.

CYCLONE GLOBAL NAVIGATION SATELLITE SYSTEM (CYGNSS)

Algorithm Theoretical Basis Document **Level 3 Soil Moisture**	**UM Doc. No.**	**148-0413**
	SwRI Doc. No.	**N/A**
	Revision	**Rev 1**
	Date	**29 October 2025**
	Contract	**NNL13AQ00C**

Prepared by: Dinan Bai, Clara Chew, Eric Small　　　　Date: 10/14/2025

Approved by: _____　　　　Date: 29 Oct 2025
　　　　Chris Ruf, CYGNSS Principal Investigator

Approved by: _____　　　　Date: 29 Oct 2025
　　　　Patrick McEnaney, CYGNSS SOC Manager

Released by: _____　　　　Date: 29 Oct 2025
　　　　Darren McKague, CYGNSS UM Project Manager

REVISION NOTICE

Document Revision History		
Revision	**Date**	**Changes**
INITIAL RELEASE	9 May 9 2019	UCAR/CU CYGNSS Soil Moisture Product User Guide supporting v1.0 product release
REVISION 1	29 Oct 2025	Update for use with V3.2 L1 reflectivity input data

Table of Contents

1   GNSS-Reflectometry Background

1.1   GNSS-R Geometry

Global Navigation Satellite System-Reflectometry (GNSS-R) is a form of bistatic radar that utilizes transmitted navigation signals as the signal source. GNSS is an umbrella term that encompasses constellations like the United States' GPS, but also the EU's Galileo, Russia's GLONASS, China's Beidou, India's IRNSS, and Japan's QZSS. In total, there are over 80 GNSS satellites currently in orbit (32 of which are GPS satellites), with more being planned in the coming years.

To date, GNSS-R most commonly utilizes signals transmitted from GPS satellites, which are circularly polarized, L-band microwave signals. Unlike monostatic radar, which measures backscatter, GNSS-R measures the forward-scattered signal, which has reflected off of the surface of the Earth and back into space. Figure 1 presents a schematic of the signal geometry. A satellite in low Earth orbit, with a GNSS-R receiver onboard, has one or more downward-looking antennas, which record the forward-scattered signals.
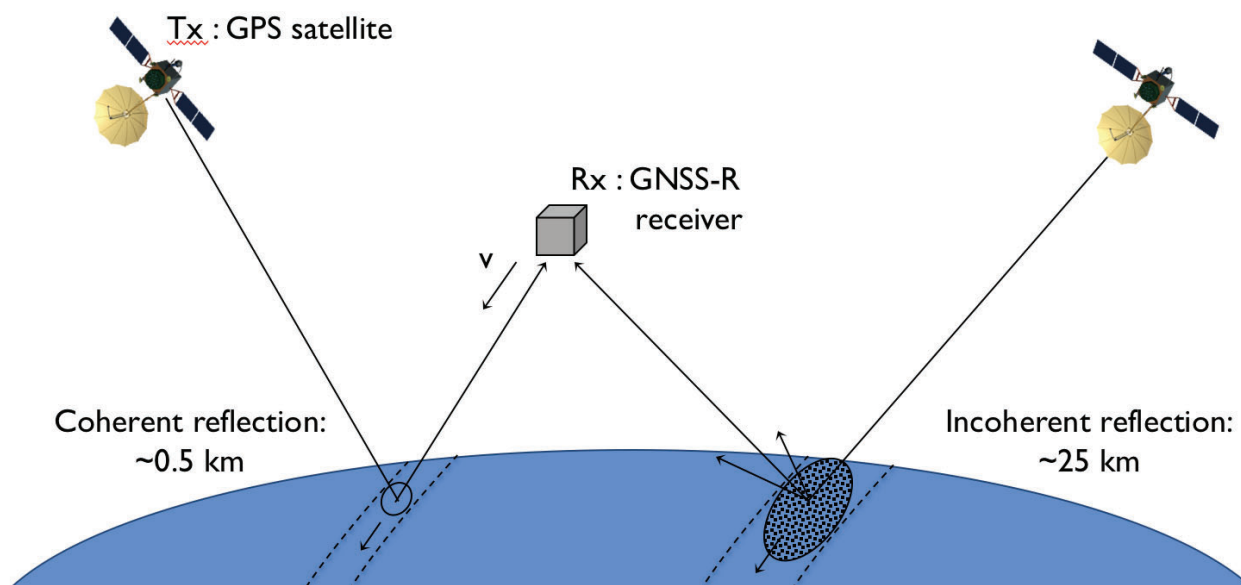
Figure 1. Schematic of the GNSS-R technique. A GNSS satellite transmits (Tx) a signal towards the Earth's surface. Part of this signal reflects in the forward (specular) direction and back into space. A GNSS-R receiver (Rx) onboards a low Earth orbiting satellite, with a downward looking antenna, records this signal. The point on the Earth's surface where the signal reflects depends upon the positions of the transmitting and receiving satellites. The roughness of the surface at the reflection point determines the spatial resolution of the signal, with rougher surfaces producing larger spatial footprints. Nearly always, the receiver integrates the reflected signal over a period of time, which elongates the spatial footprint in the along-track direction.

1.2   Revisit Time

The point of reflection on the Earth's surface is determined by the positions of the transmitting and receiving satellites. Because these positions are constantly changing, the collecting areas are pseudo-randomly distributed on the Earth's surface. This is different than traditional remote sensing techniques, which collect data in repeatable swaths. The temporal repeat time of GNSS-R is thus statistical. This means that, for a given point of the Earth's surface, observations could be recorded one hour apart, and then there could be no observations for the next several hours, for example. Observations are recorded at all times of day, again, unlike traditional remote sensing techniques, which tend to design their collection strategies to always occur at a particular location at a particular time of day. The pseudo-random distribution of observations, over time, aggregate such that complete maps of the reflected signal can be made (Figure 2).
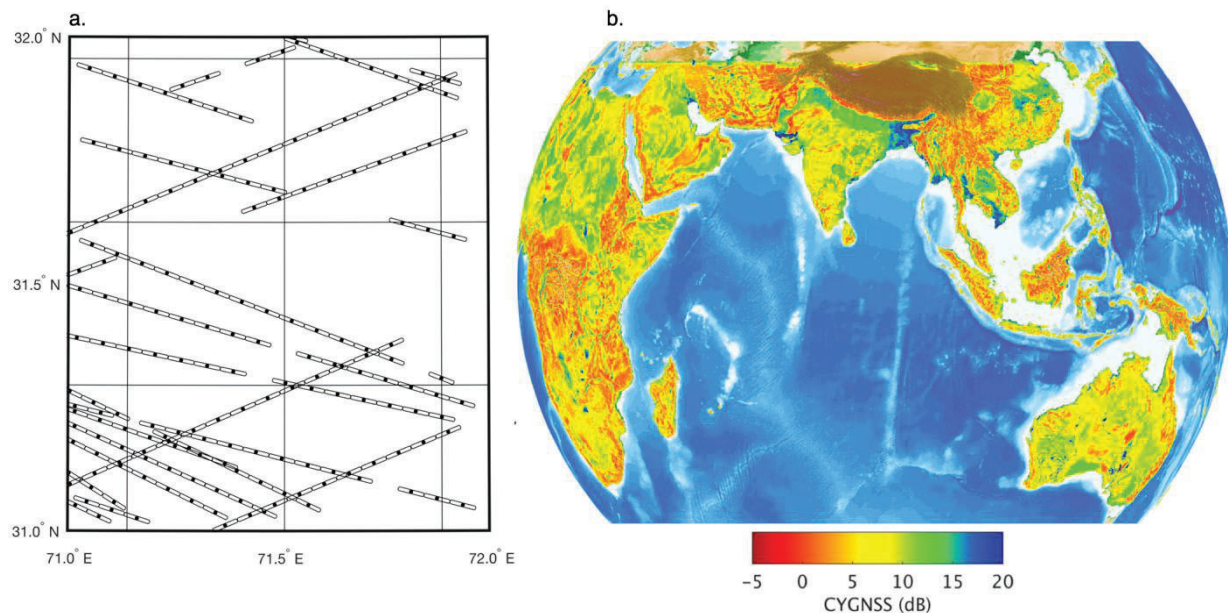

Figure 2. a. Illustration of the pseudo-random surface sampling by CYGNSS (ellipses with dots). Ellipses are approximately 3.5 x 0.5 km in size, which is the expected footprint if the surface has little surface or topographic roughness. Dots are the location of the specular reflection points recorded by CYGNSS. b. Over time, observations made by CYGNSS completely cover the land surface, producing maps such as this. Here, higher values could indicate a wet surface or a relatively flat surface.

1.3   Spatial Resolution

The spatial resolution of the reflecting signal depends on the roughness of the surface at and near the reflection point. If the surface is sufficiently rough, then the reflected signal is incoherent and comes from an area called the 'glistening zone,' which is on the order of tens of kilometers (~25 km in the case of the ocean surface). If the surface is relatively smooth, then the reflected signal is coherent and comes from an area defined by the first Fresnel zone. For a low Earth orbiting GNSS-R satellite, this area is on the order of ½ a kilometer, though this depends slightly (+/- a few

hundred meters) on incidence angle. What can be defined as a rough versus smooth surface is still a subject of debate. Theoretically at L-band, once the RMS surface roughness exceeds a few centimeters, then there should be little to no reflected signal coming from the first Fresnel zone. In practical terms, however, surface roughness is an extremely difficult parameter to measure, and surface roughness will vary considerably on scales as large as the first Fresnel zone. In all likelihood, the reflected signal for the coherent case comes from areas within the first Fresnel zone that are smooth, and most signals are probably a combination of incoherent and coherent scattering. Regardless, some studies are beginning to show that a large portion of spaceborne GNSS-R signals collected over the land surface have a coherent component (Al-Khaldi et al., 2021).

Due to the fact that CYGNSS was designed to be an ocean sensor, where the reflected signal is relatively weak, the processing software integrates the signal over a period of 0.5(1.0) second for each 'observation.' During that time, the spacecraft has moved approximately 3.57.0) km, which means that the smallest along-track spatial resolution possible over land is 3.5(7.0) km, though the across track could still be the theoretical 0.5 km. This results in the spatial footprint having a minimum size of 3.5(7.0) x 0.5 km, with the signal being smeared out along track (Figure 2). The incoherent integration time was reduced from 1.0 to 0.5 seconds in July 2019. After this change, the footprint has been approximately 3.5 km × 0.5 km.

1.4   Delay-Doppler Maps

The reflected GNSS signal is recorded by the receiver in the form of what is called a delay-Doppler map (DDM). A DDM is created by cross correlating the received signal with a locally-generated replica for different path delays (resulting from the path distance between the transmitter, reflecting surface, and receiver) and Doppler shifts (resulting from the relative motions of the transmitter, reflecting surface, and the receiver). Two examples of DDMs are shown in Figure 3. Figure 3a is an example of a DDM recorded by TDS-1 (a precursor to CYGNSS) over the land surface, and Figure 3b is an example of a DDM recorded over the ocean surface. The horseshoe shape of the ocean DDM is an indication that the reflection is incoherent and comes from a large, rough area. The lack of horseshoe in Figure 3a indicates that the reflection is mostly coherent, and comes from a smaller, smoother area. The maximum power of each DDM is affected by both surface roughness and the dielectric constant of the surface, which is explained further in Section 2.

1.5   CYGNSS Observables

DDMs are most commonly used by summarizing them into one metric or observable, though in very rare cases, the entire DDM or waveform (one slice of the DDM along constant doppler) may be used. The observables that are commonly used for soil moisture (SM) estimation are the peak cross-correlation of each DDM, or the peak divided by the noise floor (signal to noise ratio, SNR). The value of the peak of each L1a power DDM ($P_{r,eff}$) is related to surface characteristics at the specular reflection point of the GNSS signal—including the roughness of the surface and the surface dielectric constant.
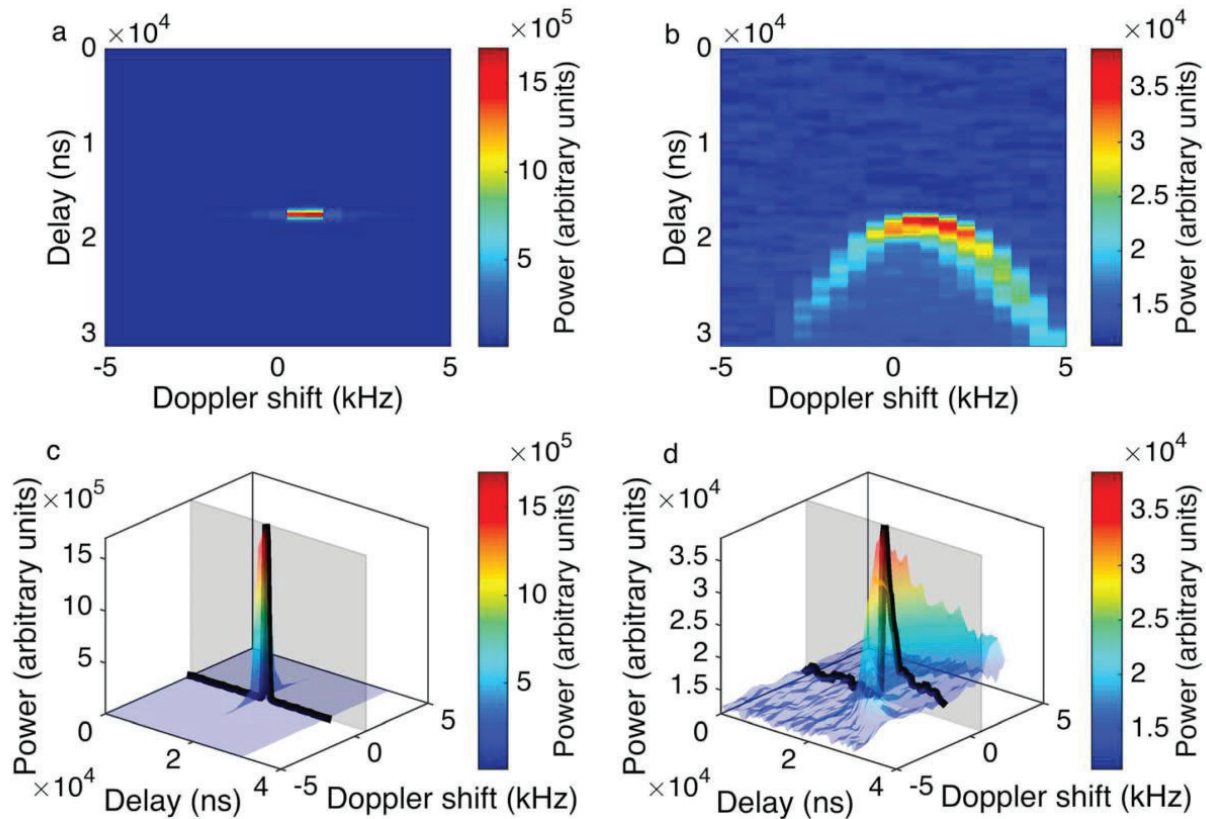
Figure 3. (a) DDM recorded over a rice field in the Ebro Delta, Spain. (b) DDM recorded over the Mediterranean Sea. (c and d) Same as Figures 1a and 1b except that also shown are the waveforms at a constant Doppler shift, indicated by the black traces. Note that the z axis scales in Figures 1b and 1d are an order of magnitude smaller than those in Figures 1a and 1c. Figure reproduced from Chew et al., 2016.

2   Soil Moisture Sensing Using GNSS-R

2.1   Previous Work

Historically, the majority of spaceborne GNSS-R studies focused on signals reflecting from the ocean surface, either for the purpose of relating ocean surface roughness to wind speed, or for altimetric applications. Ground- and aircraft-based experiments had shown success in measuring GNSS-R signals over land and relating them to changes in near-surface (0-5 cm) SM or vegetation water content, but it had generally been assumed that spaceborne GNSS-R signals recorded over the land surface would be too weak to be useful for these kinds of applications.

After the launch of TechDemoSat-1 (TDS-1) in 2014, observational evidence began to mount in favor of developing GNSS-R for land applications. Both Camps et al. (2016) and Chew et al. (2016) analyzed data from TDS-1 for sensitivity to soil SM and found spatial and temporal variations in the GNSS reflected signal that appeared to be driven by SM. Since then, both TDS-1 and the SMAP radar receiver (adapted to record GNSS-R signals) have shown sensitivity to a

variety of land surface variables including wetland extent (Nghiem et al., 2017) and surface freeze/thaw (Chew et al., 2017). Both TDS-1 and SMAP, though garnering the largest spaceborne GNSS-R datasets of their time, do not collect enough data to provide operational products and are mostly limited to proof-of-concept investigations.

NASA's Cyclone GNSS (CYGNSS) constellation, launched in December of 2016, however, does provide enough data. Instead of being a single instrument, CYGNSS is comprised of eight GNSS-R satellites in low Earth orbit around the tropics and each uses two rather than one Earth viewing antenna. This vastly decreases the temporal repeat time. For instance, for the latitudinal band ~+/-38 degrees, CYGNSS samples approximately 80% of SMAP's 36 km EASE2 grid cells every day, and most of the time CYGNSS will have multiple observations per day in every grid cell.

2.2 Remote Sensing at L-band

Data collected by CYGNSS are sensitive to near-surface SM. How strongly any signal reflects off of a surface is dependent on the dielectric constant of the surface. At L-band, the dielectric constant of the Earth is mostly controlled by its moisture content, with wetter surfaces producing stronger reflections. There is a secondary dependence on soil texture (i.e. the relative amounts of sand, silt, and clay that comprise a soil), though it is small compared to the effect from SM.

L-band is often quoted as the wavelength of choice when it comes to SM remote sensing. Higher frequencies like X- or C-band cannot penetrate even minimal vegetation canopies, whereas L-band can. L-band can penetrate the soil surface to some extent, and the amount of penetration also depends on SM (Njoku & Entekhabi, 1996). In general, the effective penetration depth of an L-band signal, and thus of GNSS-R signals, is between 0-5 cm. Longer wavelength signals, like P-band, have been studied for their ability to sense rootzone SM, though its penetration depth will also depend on moisture content, which leads to greater uncertainty in knowing at what depth the retrieved SM is actually representing. Restrictions on the transmission of this wavelength have also limited its development.

2.3 GNSS-R Sensitivity to Soil Moisture

Since 2015, there have been several studies investigating the sensitivity of GNSS-R to SM (Camps et al., 2016; Chew et al., 2016). Most of these studies were conducted using empirical observations from CYGNSS or TechDemoSat-1. Observational evidence clearly shows that GNSS-R is very sensitive to surface water from lakes and rivers (Figure 4) even in the presence of an overlying vegetation canopy.

Measuring the sensitivity of GNSS-R/CYGNSS observations to SM, however, is more challenging. Spatial variations in both land cover and topography, which affect the roughness of the surface, will also affect the power of the signal reflected from the surface in the specular direction that is received by CYGNSS, $P_{r,eff}$. This is exemplified in Figure 5, which shows a satellite image of northern India along with CYGNSS observations of $P_{r,eff}$. Although higher $P_{r,eff}$ is observed in vegetated areas, which should have higher SM than the surrounding arid regions, one can also see the influence of mountain ranges and other surface features on $P_{r,eff}$.

In order to untangle the response of $P_{r,eff}$ to both SM and land cover/surface roughness, we assume that over time only SM changes whereas land cover and surface roughness remain largely static. Of course, this approach ignores changes in vegetation water content. By looking at temporal fluctuations in both SM and $P_{r,eff}$, we can quantify the sensitivity of $P_{r,eff}$ to SM. Figure 6 shows an example of this kind of analysis in India, where changes in SMAP SM are compared to gridded changes in $P_{r,eff}$. The correlation between the two is strong (r = 0.84).

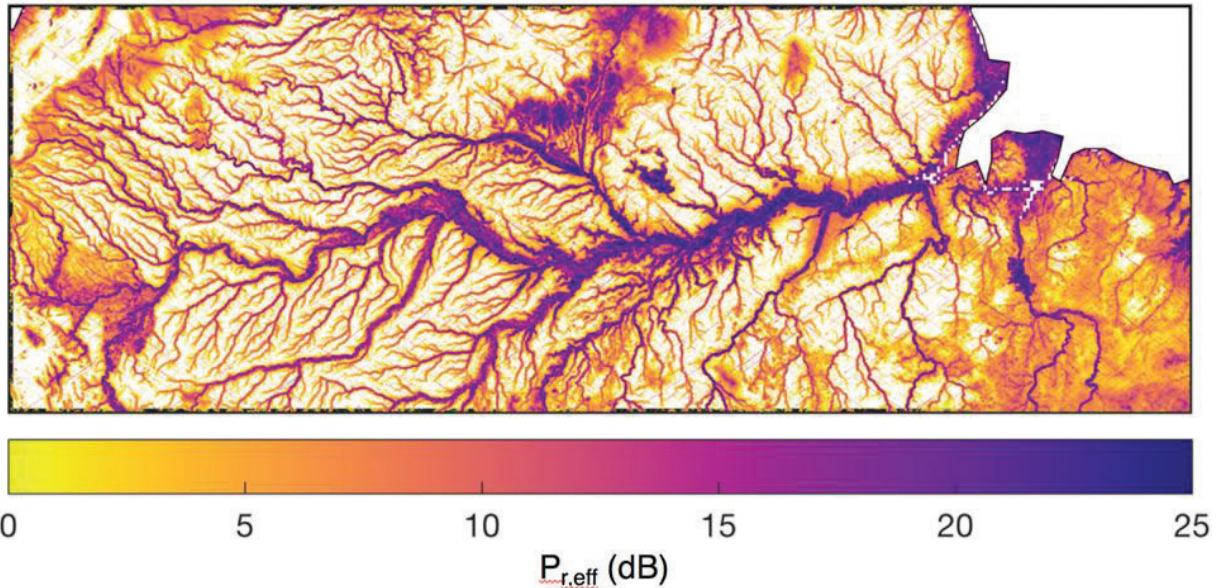Figure 4. Observations of $P_{r,eff}$ over the Amazon Basin.
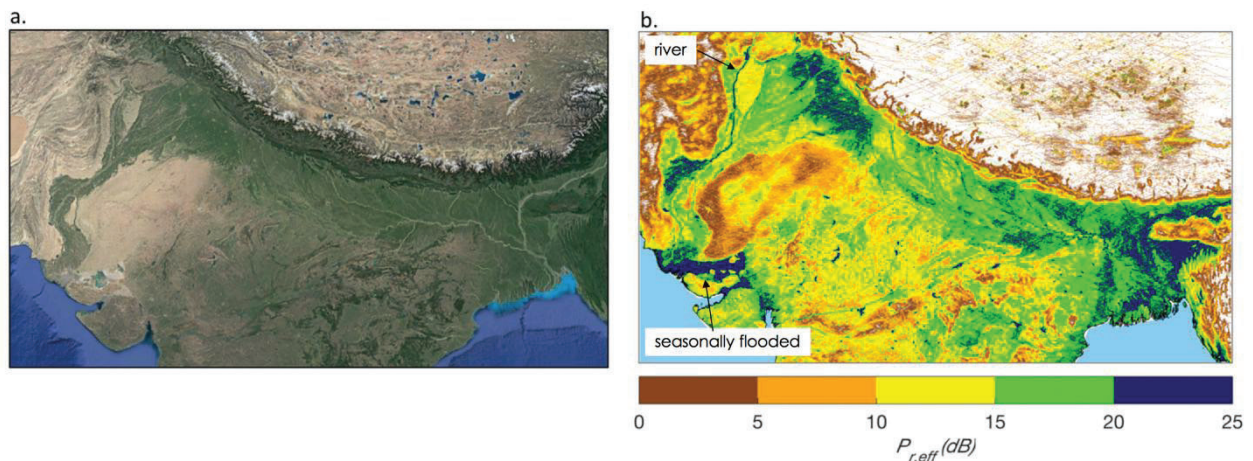

Figure 5. a. Google Earth image of northern India. b. CYGNSS observations of Pr,eff over the same region. The color scale assigned to Pr,eff is continuous and the color bar is only discretized in 5 dB steps to highlight the response of Pr,eff to different land cover types.
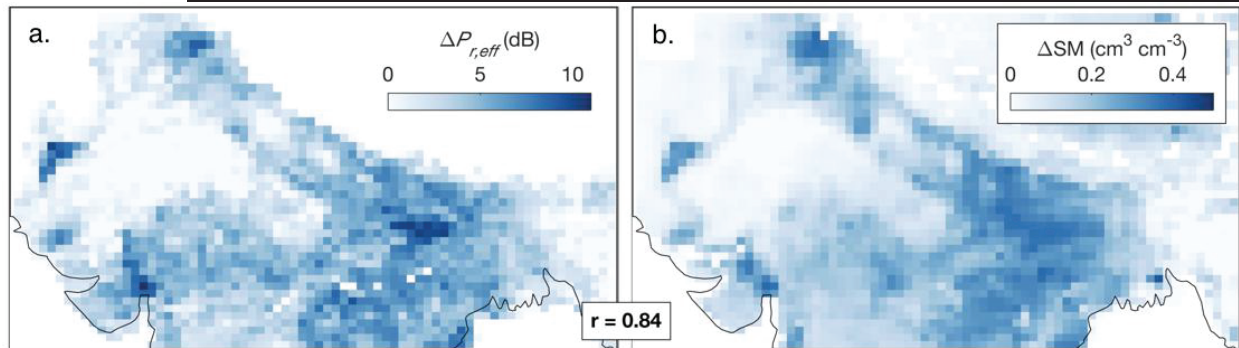
Figure 6. a. Changes in Pr,eff, gridded to 36 km, between May and August, 2017. b. Changes in soil moisture from SMAP between May and August, 2017. Adapted from Chew and Small, 2018.

3   The Level 3 Soil Moisture Retrieval Algorithm

3.1   Introduction to the Algorithm

The algorithm uses collocated SM retrievals from the Soil Moisture Active Passive (SMAP) mission as its reference against which to calibrate concurrent (same day) CYGNSS observations. For a given location, a linear relationship between SMAP SM and CYGNSS reflectivity is assumed, and the relationship is used to transform all CYGNSS observations into SM, even at times when there are no SMAP match ups available.

Using SMAP data as the reference comes with many drawbacks, the major one being that SMAP SM retrievals are not actual ground truth observations and hence have their own errors and uncertainties. One must be careful when using CYGNSS data in areas where it is known that SMAP performs poorly. In addition, SMAP's 40 km spatial resolution is likely much coarser than that of CYGNSS. Intelligent upscaling of CYGNSS data to the 36 km EASE grid that SMAP uses is necessary. If the resolution of CYGNSS is smaller than 36 km, then we are in effect degrading the CYGNSS data by doing this and are not using it to its full potential. A finer resolution 9 km version of the CYGNSS SM product is also provided in an attempt to recover some of the spatially varying information that is lost in the 36 km upscaling process.

3.2   Data Sets

3.2.1   CYGNSS Level 1 data.

CYGNSS, a constellation of eight smallsats, measures specular bistatic scattering of GNSS signals from the Earth surface and provides global coverage between 38°S and 38°N with a mean revisit time of approximately 7 hours (Ruf et al., 2022). Under fully coherent scattering conditions (Camps, 2020), each specular reflection measurement corresponds to an approximate footprint of 7 km × 0.5 km prior to July 2019, when the incoherent integration time was reduced from 1.0 to 0.5 seconds. After this change, the footprint was halved to approximately 3.5 km × 0.5 km. The CYGNSS L1 dataset provides calibrated GNSS-R observables derived from raw measurements

and associated metadata, typically with a latency of six days. The latest Version 3.2 L1 data spans from 1 August 2018 to the present. Compared to the previous Version 2.1 release, V3.2 introduces several key calibration improvements, including corrections to the Delay Doppler Map (DDM) noise floor (Gleason et al., 2022), compensation for thermal effects in system electronics (Al-Khaldi et al., 2025), and a new dynamic Equivalent Isotropic Radiated Power (EIRP) estimation algorithm (Wang et al., 2022). In addition, an expanded set of quality flags has been implemented. The new CYGNSS SM product is named V3.2 to align with the updated L1 dataset version.

3.2.2 SMAP Soil Moisture

The SMAP mission measures top-layer (0–5 cm) surface SM using an L-band passive radiometer, with observations collected at 6 a.m. (descending orbit) and 6 p.m. (ascending orbit) local solar time, and a revisit time of 2–3 days. For this study, we use SMAP Level-3 Radiometer Global Daily SM products at both 36 km and enhanced 9 km resolutions, covering the period from August 1, 2018, to December 31, 2024. Specifically, we select descending-orbit observations using the Dual-Channel Algorithm (DCA), which has shown improved performance due to thermal equilibrium conditions at the local acquisition time (O'Neill et al., 2020).

3.2.3 Ancillary Data

To exclude CYGNSS specular observations near or over open water, a static water mask is applied prior to SM retrieval. This mask is derived from the Global Surface Water Explorer (GSWE) dataset (Pekel et al., 2016), which provides 30-meter resolution global water body classifications based on long-term Landsat observations using optical remote sensing. Measurements located on or near open water surfaces are removed and not used to retrieve SM.

3.3 Algorithm Description

This section is a step-by-step guide to the SM retrieval algorithm. It assumes a working knowledge of the CYGNSS Level 1, version 3.2, netcdf files, all of which are available here: https://podaac.jpl.nasa.gov/dataset/CYGNSS_L1_V3.2). In general, for every day of the year there will be eight Level 1 files, one for each CYGNSS satellite. Each of the eight files contains information pertaining to the thousands of reflections recorded on that day. The following steps are applied to each reflection in each file.

3.3.1 Surface Effective Reflectivity

GNSS-R land scattering models have been extensively studied in previous works (Campbell et al., 2022; Tsang et al., 2022). The primary GNSS-R Level-1 observable is the Delay Doppler Map (DDM), which measures received signal power across a range of propagation time delays and Doppler frequencies. In the forward model, the DDM received power $P_{r,eff}$ at the specular bin is composed of coherent (P_c) and incoherent (P_i) components:

$$P_{r,eff} = P_c + P_i \tag{1}$$

where

$$P_c = \frac{\lambda^2 P_T G_T G_R}{(4\pi)^2 (R_T + R_R)^2} \cdot \Gamma_e \tag{2}$$

$$P_i = \frac{\lambda^2 P_T G_T G_R}{(4\pi)^3 (R_T \cdot R_R)^2} \cdot \sigma_b \tag{3}$$

where λ represents the GNSS wavelength ($\approx 0.19\ cm$); $P_T G_T$ is the GNSS transmitter's EIRP; and R_T and R_R are the distances from the transmitter and receiver to the specular point, respectively. The terms Γ_e and σ_b represent the surface Effective Reflectivity and the Bistatic Radar Cross Section (BRCS), respectively, and are the two key quantities describing the surface scattering properties that are related to soil moisture.

CYGNSS operational L1 DDMs measure the total receiver power and do not separate coherent and incoherent components, making it difficult to independently estimate Γ_e and σ_b under mixed scattering conditions over land. Several studies have shown that either σ_b (Al-Khaldi et al., 2019) or Γ_e (Chew & Small, 2020) can serve as a suitable observable for SM retrieval, depending on the assumed dominant scattering regime. The science community continues to investigate GNSS-R land coherence characteristics (Al-Khaldi et al., 2021; Balakhder et al., 2019). A full discussion of land scattering coherence is beyond the scope of this document. In the V3.2 SM product, we adopt Effective Reflectivity as the primary observable, assuming the coherent component is dominant. This assumption is consistent with the approach used by Chew & Small (Chew & Small, 2020) in the CYGNSS V1.0 SM retrieval algorithm.

Continuing with the forward model, the surface Effective Reflectivity in equation (2) can be expressed as:

$$\Gamma_e = |\Re(\theta_i, \epsilon)|^2 \cdot \gamma_{RN} \cdot \gamma_{VG} \tag{4}$$

where $|\Re(\theta_i, \epsilon)|^2$ is the Fresnel Coefficient for Right-hand Circular Polarized (RHCP) incident waves and Left-hand Circular Polarized (LHCP) scattered waves. This coefficient depends on the incidence angle θ_i and soil permittivity ϵ, which is a function of volumetric water content inside the soil and soil texture (Mironov et al., 2009). The terms γ_{RN} and γ_{VG} represent attenuation from surface roughness and vegetation, respectively.

Under the assumption of negligible P_i, the surface Effective Reflectivity Γ_e can be estimated directly from the measured DDM peak power $P_{r,eff}$ by inverting equation (2):

$$\Gamma_e = \frac{(4\pi)^2}{\lambda^2} \cdot \frac{(R_T + R_R)^2}{P_T G_T G_R} \cdot P_{r,eff} \tag{5}$$

Here, the DDM received power $P_{r,eff}$ is used to represent the specular power. The CYGNSS V3.2 L1 calibration includes updates to the dynamic EIRP algorithm, the corrections to the Delay Doppler Map (DDM) noise floor and thermal effects of system electronics. It improves the accuracy of $P_T G_T$ and $P_{r,eff}$, providing a more reliable estimate of Γ_e.

3.3.2 Incidence Angle Correction

Incidence angle is also expected to affect coherent reflection. Previous work (Chew & Small, 2022) shows that Γ_e exhibits an incidence angle dependence which becomes significant above ~50° (figure 7). This is consistent with the Fresnel coefficient model. We compared the mean, modeled relationship to observations of Γ_e and confirmed the overall drop in Γ_e as incidence angle increases beyond 40 degrees (Figure 7 right). To account for this, Γ_e is normalized to its value at nadir (Γ_{en}), using a modeled angle-dependence curve $f(\theta)$ derived from the Fresnel Coefficient, following methods in (Al-Khaldi et al., 2019; Chew & Small, 2022):

$$\Gamma_{en} = \frac{\Gamma_e}{f(\theta)} \tag{6}$$

The resulting angle-normalized Effective Reflectivity, Γ_{en}, is used as the input to the CYGNSS SM retrieval model.
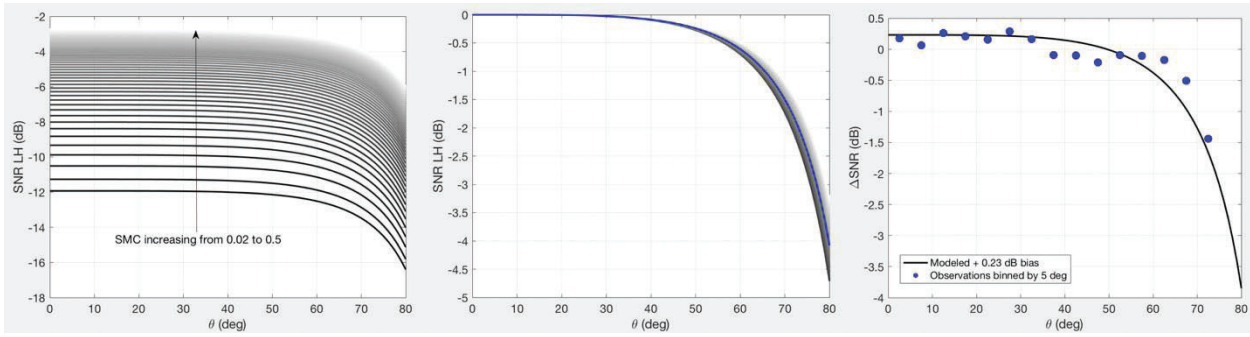

Figure 7. (left) Modeled relationship for how Pr,eff varies with incidence angle and soil moisture. (middle) Same as the left-hand panel, though here modeled Pr,eff has been normalized to show that soil moisture does not significantly change the relationship between Pr,eff and incidence angle. The blue line is the mean of the normalized relationships. (right) We binned observations of Pr,eff over the Sahara in 5 degree increments to confirm that the modeled relationship at least loosely resembles what is seen in the observations.

3.3.3 Level 3 Soil Moisture Retrieval Model and Product

According to the surface Effective Reflectivity model in equation (4), the inversion of SM from Γ_{en} requires additional surface information, including roughness, vegetation characteristics, and soil texture. However, existing ancillary datasets typically lack the spatial resolution and temporal variability necessary to accurately represent the electromagnetic scattering parameters in the GNSS-R forward model. As a result, an empirical approach is adopted. A linear regression model is derived from collocated and concurrent observations of CYGNSS measured Γ_{en} and SMAP L3 36 km SM. This empirical linearity reflects a first-order approximation of equation (4), with surface and vegetation effects implicitly captured in the regression parameters.
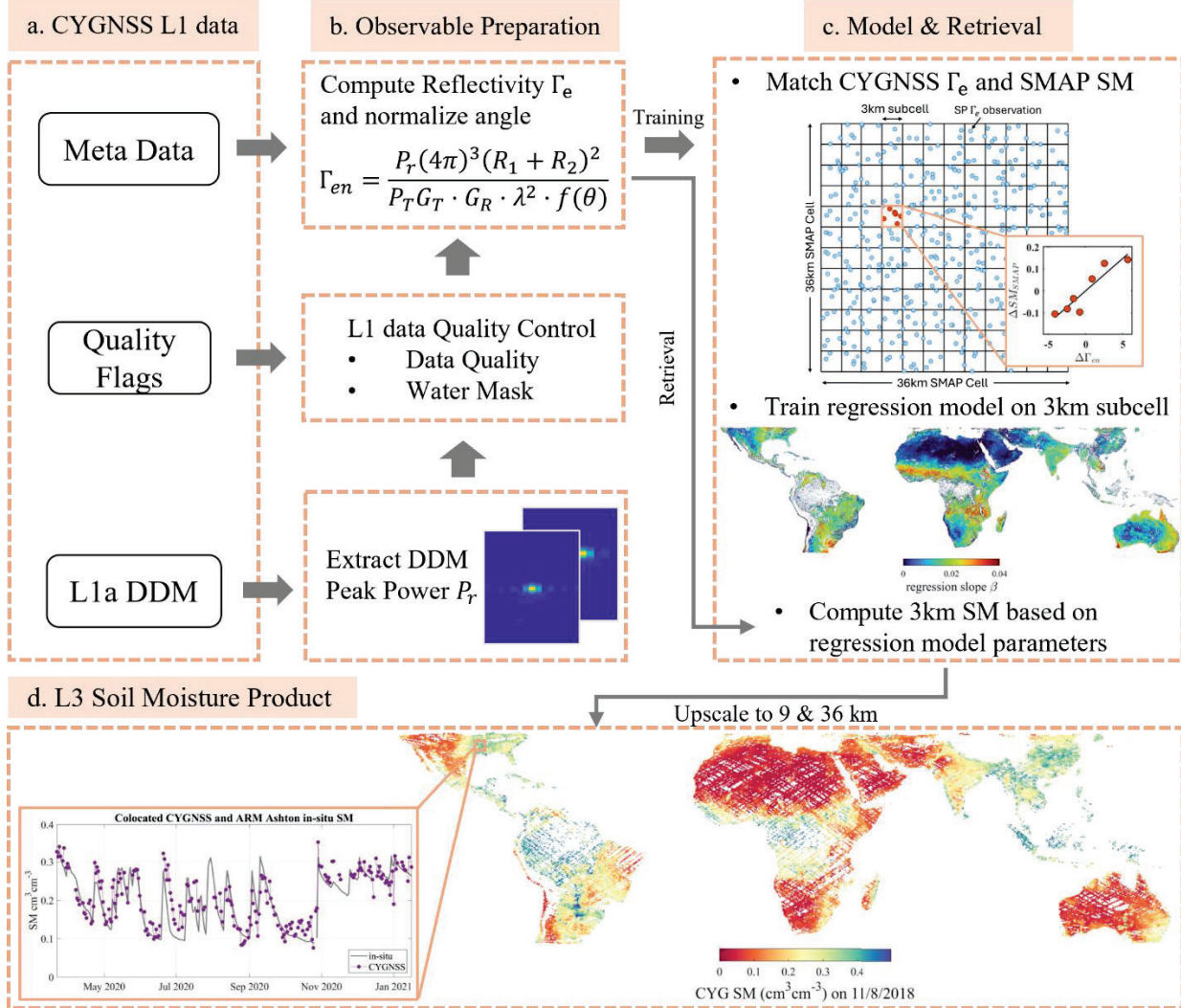
Figure 8. Schematic diagram of CYGNSS V3.2 L3 SM retrieval model training and daily SM retrieval.

The model development and retrieval process are summarized in Figure 8. First, CYGNSS L1 measurements are filtered using a set of quality control flags. Compared to the Version 1.0 retrieval model, additional quality flags are introduced in Version 3.2 to better exclude anomalous land observations. A static water mask derived from the GSWE dataset is also applied, removing specular points located over open water or areas where the water fraction within a 5 km radius exceeds 1%. SMAP L3 observations labeled as "Retrieval Successful" are selected for use as the reference during model training. Details of the quality control procedures applied in both the V1.0 and V3.2 retrieval models are summarized in Table 1.

Next, Γ_{en} is estimated from the filtered L1 DDM and associated metadata. For each collocated SMAP L3 36 km observation, all CYGNSS measured Γ_{en} within a ±12-hour time window are collected and spatially binned into 3 km subcells, as illustrated in Figure 8. The 3 km resolution is consistent with the approximate footprint of CYGNSS measurements under coherent scattering

conditions. Within each 3 km subcell, land cover and surface conditions are assumed to be statistically homogeneous, allowing the linear relationship between Γ_{en} and SM to hold locally.

The regression model is trained using data from 1 August 2018 (the beginning of Version 3.2 L1 data) to 15 November 2023. This five-year span provides sufficient CYGNSS and SMAP matchups to capture the seasonal and interannual variability in both soil moisture and Γ_{en}. The spatial distribution of the number of matched CYGNSS–SMAP observations per 3 km subcell is shown in Figure 9, with a global average of approximately 40 matchups per subcell. Within each subcell, a linear regression is performed between collocated Γ_{en} (feature) and SMAP soil moisture (label), after removing their respective mean values. The resulting slope parameter varies spatially and reflects differences in land cover, vegetation, and terrain, as shown in Figure 8. However, in arid regions where soil moisture variability is low, its estimation can be unstable due to noise in the SMAP observations (Chew & Small, 2020).

The retrieval model parameters in each 3 km subcell consist of the slope β, and the mean values of CYGNSS Γ_{en} ($\overline{\Gamma_{en}}$) and SMAP L3 SM ($\overline{SM_{smap}}$) inside the training period. The CYGNSS retrieval is then calculated as:

$$SM_{cyg} = \beta \cdot (\Gamma_{en} - \overline{\Gamma_{en}}) + \overline{SM_{smap}} \qquad (7)$$

The 36 km CYGNSS L3 SM product is generated by averaging all valid 3 km retrievals within each 36 km EASE grid cell over a given time window. As with V1.0, both daily (24-hour) and sub-daily (6-hour) retrievals are generated. One example of the CYGNSS 36 km SM product retrieved on 8 November 2018 is shown in the bottom panel of Figure 8. A zoom-in panel on the left presents a one-year time series comparison between CYGNSS SM and in-situ measurements from the ISMN ARM Ashton station within the same 36 km grid cell, demonstrating their agreement with SM variability. In addition, Version 3.2 introduces a high-resolution 9 km product by averaging the 3 km retrievals falling within each 9 km EASE grid cell.
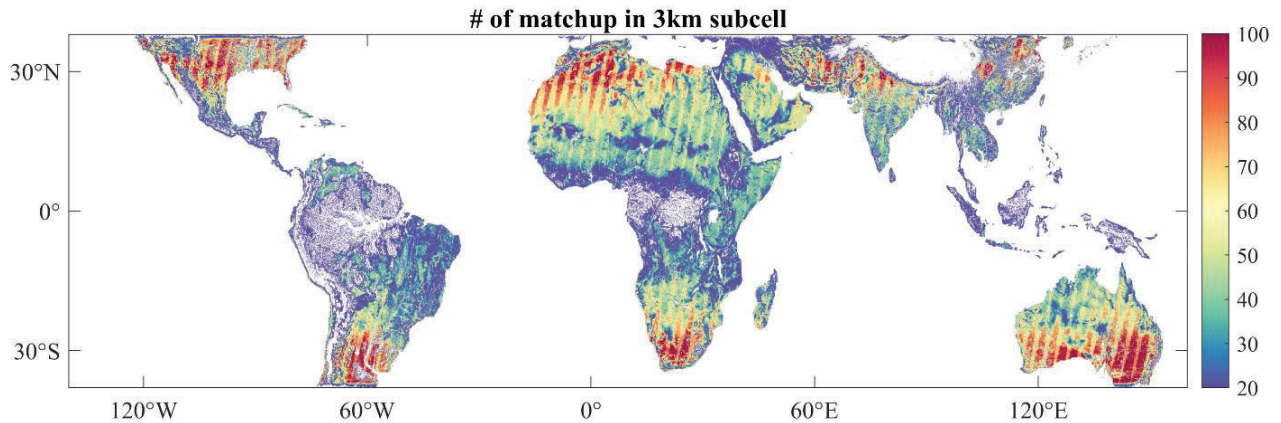
Figure 9. Number of spatiotemporally matched CYGNSS Γ_en and SMAP L3 SM in each 3 km subcell

Table 1 Summary of CYGNSS L1 data quality controls for V1.0 and V3.2 SM retrieval

	CYGNSS V1.0	**CYGNSS V3.2**
Model Input	L1 Science Data Record V2.1	L1 Science Data Record V3.2
	V2.1 Power DDM	V3.2 Power DDM
	Static EIRP	Dynamic EIRP
CYGNSS L1 data quality control	quality flags 1: bit 2, 4, 5, 8, 16, 17 (not set)	quality flags 1: bit 2, 4, 5, 6, 8, 9, 15, 16, 17, 22, 23, 25, 26, 27, 29, 30 (not set)
	Delay bin <= 7-10 pixel	quality flag 2: bit 1, 3, 4, 7, 8, 9, 13, 14, 16 (not set)
	SNR <= antenna gain+14 dB	
	Antenna gain > 0 dB	
	SNR > 2 dB	SNR > 2 dB
	Incidence angle < 65°	Incidence angle < 65°
SMAP L3 quality	None	flag bit 3 Retrieval Successful
Water Mask	No water at specular	No water at specular
	Water in 7 by 7 km rectangular region around Specular < 1%	Water in 5 km radius circular region around Specular < 1%
SMAP and CYGNSS temporal matchup	Same calendar day	CYGNSS reflectivity sampled within SMAP sample time ±12 hours
Model Training Period	17 Mar 2017 to 1 Oct 2018	1 Aug 2018 to 15 Nov 2023
Product spatial resolution	36 km	9 & 36 km

3.4   Product Quality Control

Currently, quality control is minimal. We are planning to add static and dynamic quality flags in an upcoming version.

4   Performance Assessment

4.1   Validation with SMAP Soil Moisture

Scatter density plots of all CYNGSS and SMAP SM pairs (9 and 36 km products) are shown in Figure 10, where the black dashed lines indicate the 1:1 line of perfect agreement. For the 36 km resolution products, CYGNSS and SMAP exhibit a strong correlation of 0.92 and an RMSD of 0.047 cm³/cm³. For the 9 km products, the correlation is 0.89 with an RMSD of 0.052 cm³/cm³. The density distribution reveals that the majority of SM values from both products fall within the low moisture regime (<0.15 cm³/cm³), while higher values are less frequent, as they typically occur in response to precipitation and hydrologic conditions.
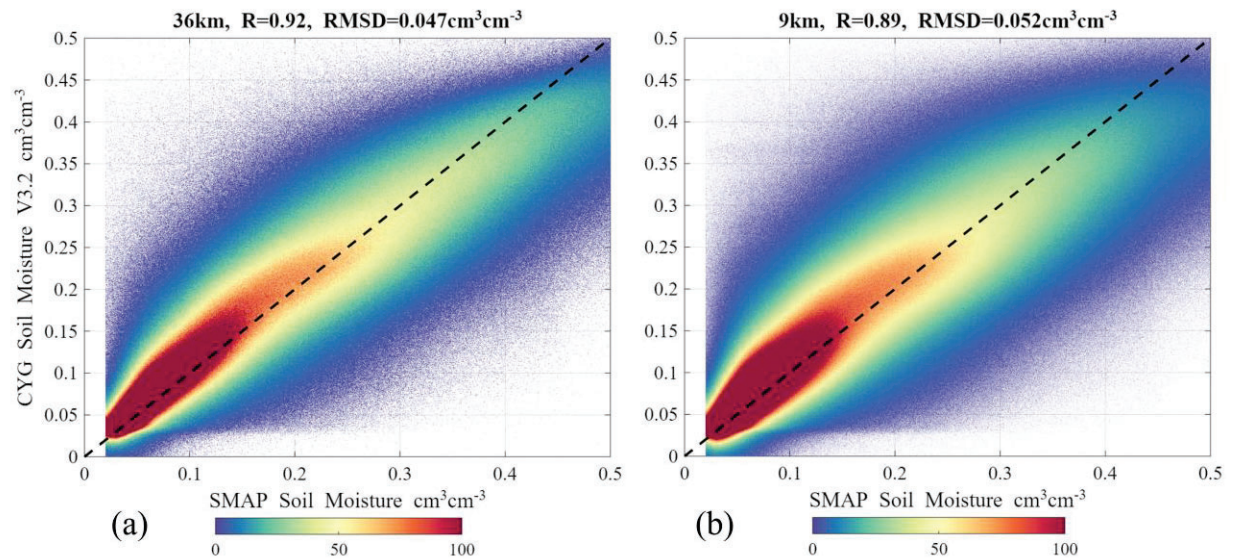
Figure 10. Scatter Density plot of CYGNSS V3.2 SM vs SMAP SM product at (a) 36 km and (b) 9 km resolutions.

4.2   Validation with in-situ Soil Moisture

Ground-based in-situ SM measurements used for validation are obtained from the International Soil Moisture Network (ISMN) (Dorigo et al., 2021). This study includes data from eight ISMN sub-networks: ARM (Cook, 2016), OZNET (Smith et al., 2012), SCAN (Schaefer et al., 2007), SNOTEL (Leavesley et al., 2008), SoilSCAPE (Moghaddam et al., 2010), USCRN (Bell et al., 2013), TAHMO (van de Giesen et al., 2014), and TxSON (Caldwell et al., 2019), comprising a total of 288 stations. Only measurements from sensors located in the topsoil layer (0–5 cm) and labeled as "high quality" are used. To match the temporal resolution of satellite-based products, hourly in-situ data are averaged to a daily scale.

The overall performance of CYGNSS SM products compared against selected ISMN networks is summarized in Table 2. For each product, the median values of correlation, bias, RMSD, and unbiased RMSD (ubRMSD) are reported across all networks. Overall, the V3.2 36 km and 9 km products demonstrate improved performance relative to the V1.0 product. Specifically, correlation increases by approximately 11% and 4% for the 36 km and 9 km products, respectively, while RMSD and ubRMSD decrease by 6.1% and 7.7% across both resolutions. At the individual network level, the V3.2 36 km product shows consistent improvements over V1.0 for all networks. However, performance across all versions remains limited in networks located in complex terrain, such as SNOTEL.

Table 2 Summary of retrieval performances' medians against in-situ SM of each ISMN Network

Network	Number of matchups	SM products	R	Bias $[cm^3 cm^{-3}]$	RMSD $[cm^3 cm^{-3}]$	ubRMSD $[cm^3 cm^{-3}]$
ARM	17	CYG V1.0 36 km	0.674	-0.039	0.076	0.044
		CYG V3.2 36 km	0.725	-0.018	0.066	0.038
		CYG V3.2 9 km	0.692	-0.014	0.066	0.037
OZNET	18	CYG V1.0 36 km	0.561	0.016	0.074	0.040
		CYG V3.2 36 km	0.635	0.047	0.077	0.043
		CYG V3.2 9 km	0.588	0.049	0.080	0.048
SCAN	109	CYG V1.0 36 km	0.455	0.008	0.085	0.041
		CYG V3.2 36 km	0.512	0.013	0.081	0.039
		CYG V3.2 9 km	0.461	0.013	0.081	0.038
SNOTEL	27	CYG V1.0 36 km	0.124	-0.039	0.122	0.055
		CYG V3.2 36 km	0.137	-0.016	0.115	0.050
		CYG V3.2 9 km	-0.004	-0.047	0.120	0.036
SOILSCAPE	31	CYG V1.0 36 km	0.446	-0.049	0.059	0.026
		CYG V3.2 36 km	0.479	-0.019	0.042	0.025
		CYG V3.2 9 km	0.490	-0.021	0.046	0.025
TxSON	40	CYG V1.0 36 km	0.631	-0.015	0.060	0.032
		CYG V3.2 36 km	0.686	0.011	0.064	0.032
		CYG V3.2 9 km	0.616	0.009	0.068	0.036
USCRN	42	CYG V1.0 36 km	0.458	0.013	0.082	0.038
		CYG V3.2 36 km	0.528	0.036	0.086	0.034
		CYG V3.2 9 km	0.502	0.030	0.079	0.035
All	288	CYG V1.0 36 km	0.491	-0.005	0.082	0.039
		CYG V3.2 36 km	0.546	0.009	0.077	0.036
		CYG V3.2 9 km	0.510	0.008	0.077	0.036

5 Product File Overview:

Spatial coverage:	N: 38, S: -38 E: 164, W: -135	**Data format:**	netCDF4
Spatial resolution:	36 km x 36 km, 9 km x 9 km	**Platform:**	CYGNSS
Temporal coverage:	Aug 1st, 2018, to present	**Sensor:**	CYGNSS GNSS-R receivers
Temporal resolution:	6 hours, 24 hours	**Version:**	V3.2
Data contributors:	Dinan Bai, Clara Chew, Eric Small		

The CYGNSS Level 3 Soil Moisture v3.2 dataset provides a daily product with two files (9 km and 36 km). Each NetCDF file contains the following variables:

Variable	Description	Dimensions (36 km)	Dimensions (9 km)
latitude	Latitude of the center of each grid cell	252 × 802	1004 × 3204
longitude	Longitude of the center of each grid cell	252 × 802	1004 × 3204
timeintervals	Start and stop times for subdaily soil moisture retrievals (e.g., (0,6) means 0–6 h)	4 × 2	4 × 2
SM_daily	Average soil moisture for each grid cell over the full 24 h period	252 × 802	1004 × 3204
SM_subdaily	Average soil moisture for each grid cell during each specified time interval	4 × 252 × 802	4 × 1004 × 3204
SIGMA_daily	Standard deviation of soil moisture for each grid cell over the full 24 h period	252 × 802	1004 × 3204
SIGMA_subdaily	Standard deviation of soil moisture for each grid cell during each specified time interval	4 × 252 × 802	4 × 1004 × 3204

6 Reference

Al-Khaldi, M. M., Johnson, J. T., O'Brien, A. J., Balenzano, A., & Mattia, F. (2019). Time-Series Retrieval of Soil Moisture Using CYGNSS. *IEEE Transactions on Geoscience and Remote Sensing*, *57*(7), 4322–4331. https://doi.org/10.1109/TGRS.2018.2890646

Al-Khaldi, M. M., Johnson, J. T., Gleason, S., Loria, E., O'Brien, A. J., & Yi, Y. (2021). An Algorithm for Detecting Coherence in Cyclone Global Navigation Satellite System Mission Level-1 Delay-Doppler Maps. *IEEE Transactions on Geoscience and Remote Sensing*, *59*(5), 4454–4463. https://doi.org/10.1109/TGRS.2020.3009784

Al-Khaldi, M. M., Gleason, S., Ruf, C., McKague, D. S., Wang, T., Russel, A., & Twigg, D. (2025). Quantifying and Correcting Thermally Driven Oscillations in CYGNSS Real-Time GPS Effective Isotropic Radiated Power. *IEEE Transactions on Geoscience and Remote Sensing*, 1–1. https://doi.org/10.1109/TGRS.2025.3538681

Balakhder, A. M., Al-Khaldi, M. M., & Johnson, J. T. (2019). On the Coherency of Ocean and Land Surface Specular Scattering for GNSS-R and Signals of Opportunity Systems. *IEEE Transactions on Geoscience and Remote Sensing*, *57*(12), 10426–10436. https://doi.org/10.1109/TGRS.2019.2935257

Bell, J. E., Palecki, M. A., Baker, C. B., Collins, W. G., Lawrimore, J. H., Leeper, R. D., et al. (2013). U.S. Climate Reference Network Soil Moisture and Temperature Observations. https://doi.org/10.1175/JHM-D-12-0146.1

Caldwell, T. G., Bongiovanni, T., Cosh, M. H., Jackson, T. J., Colliander, A., Abolt, C. J., et al. (2019). The Texas Soil Observation Network:A Comprehensive Soil Moisture Dataset for

Remote Sensing and Land Surface Model Validation. *Vadose Zone Journal*, *18*(1), 190034. https://doi.org/10.2136/vzj2019.04.0034

Campbell, J. D., Akbar, R., Bringer, A., Comite, D., Dente, L., Gleason, S. T., et al. (2022). Intercomparison of Electromagnetic Scattering Models for Delay-Doppler Maps Along a CYGNSS Land Track With Topography. *IEEE Transactions on Geoscience and Remote Sensing*, *60*, 1–13. https://doi.org/10.1109/TGRS.2022.3210160

Camps, A. (2020). Spatial Resolution in GNSS-R Under Coherent Scattering. *IEEE Geoscience and Remote Sensing Letters*, *17*(1), 32–36. https://doi.org/10.1109/LGRS.2019.2916164

Camps, A., Park, H., Pablos, M., Foti, G., Gommenginger, C. P., Liu, P.-W., & Judge, J. (2016). Sensitivity of GNSS-R spaceborne observations to soil moisture and vegetation. *IEEE Journal of Selected Topics in Applied Earth Observations and Remote Sensing*, *9*(10), 4730–4742.

Chew, C., & Small, E. (2020). Description of the UCAR/CU Soil Moisture Product. *Remote Sensing*, *12*(10), 1558. https://doi.org/10.3390/rs12101558

Chew, C., & Small, E. (2022). UCAR/CU CYGNSS Soil Moisture Product User Guide.

Chew, C., Shah, R., Zuffada, C., Hajj, G., Masters, D., & Mannucci, A. J. (2016). Demonstrating soil moisture remote sensing with observations from the UK TechDemoSat-1 satellite mission. *Geophysical Research Letters*, *43*(7), 3317–3324. https://doi.org/10.1002/2016GL068189

Chew, C., Lowe, S., Parazoo, N., Esterhuizen, S., Oveisgharan, S., Podest, E., et al. (2017). SMAP radar receiver measures land surface freeze/thaw state through capture of forward-scattered

L-band signals. *Remote Sensing of Environment*, *198*, 333–344. https://doi.org/10.1016/j.rse.2017.06.020

Cook, D. R. (2016). *Soil Temperature and Moisture Profile (STAMP) System Handbook* (No. DOE/SC-ARM-TR--186). ARM Climate Research Facility, Pacific Northwest National Laboratory, Richland, WA. https://doi.org/10.2172/1332724

Dorigo, W., Himmelbauer, I., Aberer, D., Schremmer, L., Petrakovic, I., Zappa, L., et al. (2021). The International Soil Moisture Network: serving Earth system science for over a decade. *Hydrology and Earth System Sciences*, *25*(11), 5749–5804. https://doi.org/10.5194/hess-25-5749-2021

van de Giesen, N., Hut, R., & Selker, J. (2014). The Trans-African Hydro-Meteorological Observatory (TAHMO). *WIREs Water*, *1*(4), 341–348. https://doi.org/10.1002/wat2.1034

Gleason, S., Al-Khaldi, M. M., Ruf, C. S., McKague, D. S., Wang, T., & Russel, A. (2022). Characterizing and Mitigating Digital Sampling Effects on the CYGNSS Level 1 Calibration. *IEEE Transactions on Geoscience and Remote Sensing*, *60*, 1–12. https://doi.org/10.1109/TGRS.2021.3120026

Leavesley, G. H., David, O., Garen, D. C., Lea, J., Marron, J. K., Pagano, T. C., et al. (2008). A Modeling Framework for Improved Agricultural Water Supply Forecasting (Vol. 2008, pp. C21A-0497). Presented at the AGU Fall Meeting Abstracts. Retrieved from https://ui.adsabs.harvard.edu/abs/2008AGUFM.C21A0497L

Mironov, V. L., Kosolapova, L. G., & Fomin, S. V. (2009). Physically and Mineralogically Based Spectroscopic Dielectric Model for Moist Soils. *IEEE Transactions on Geoscience and Remote Sensing*, *47*(7), 2059–2070. https://doi.org/10.1109/TGRS.2008.2011631

Moghaddam, M., Entekhabi, D., Goykhman, Y., Li, K., Liu, M., Mahajan, A., et al. (2010). A Wireless Soil Moisture Smart Sensor Web Using Physics-Based Optimal Control: Concept and Initial Demonstrations. *IEEE Journal of Selected Topics in Applied Earth Observations and Remote Sensing*, *3*(4), 522–535. https://doi.org/10.1109/JSTARS.2010.2052918

Nghiem, S. V., Zuffada, C., Shah, R., Chew, C., Lowe, S. T., Mannucci, A. J., et al. (2017). Wetland monitoring with Global Navigation Satellite System reflectometry. *Earth and Space Science*, *4*(1), 16–39. https://doi.org/10.1002/2016EA000194

Njoku, E. G., & Entekhabi, D. (1996). Passive microwave remote sensing of soil moisture. *Journal of Hydrology*, *184*(1), 101–129. https://doi.org/10.1016/0022-1694(95)02970-2

O'Neill, P., Bindlish, R., Chan, S., Chaubell, M. J., Njoku, E., & Jackson, T. (2020, August 31). Algorithm Theoretical Basis Document Level 2 & 3 Soil Moisture (Passive) Data Products. Jet Propulsion Laboratory, California Institute of Technology. Retrieved from https://smap.jpl.nasa.gov/system/internal_resources/details/original/484_L2_SM_P_ATBD_rev_F_final_Aug2020.pdf

Pekel, J.-F., Cottam, A., Gorelick, N., & Belward, A. S. (2016). High-resolution mapping of global surface water and its long-term changes. *Nature*, *540*(7633), 418–422. https://doi.org/10.1038/nature20584

Ruf, C., McKague, Darren, Posselt,Derek, Gleason, Scott, Clarizia, Maria-Paola, Zavorotny, Valery, et al. (2022). *CYGNSS Handbook*. Michigan Publishing Services. https://doi.org/10.3998/mpub.12741920

Schaefer, G. L., Cosh, M. H., & Jackson, T. J. (2007). The USDA Natural Resources Conservation Service Soil Climate Analysis Network (SCAN). https://doi.org/10.1175/2007JTECHA930.1

Smith, A. B., Walker, J. P., Western, A. W., Young, R. I., Ellett, K. M., Pipunic, R. C., et al. (2012). The Murrumbidgee soil moisture monitoring network data set. *Water Resources Research*, *48*(7). https://doi.org/10.1029/2012WR011976

Tsang, L., Liao, T.-H., Gao, R., Xu, H., Gu, W., & Zhu, J. (2022). Theory of microwave remote sensing of vegetation effects, SoOp and rough soil surface backscattering. *Remote Sensing*, *14*(15), 3640.

Wang, T., Ruf, C. S., Gleason, S., O'Brien, A. J., McKague, D. S., Block, B. P., & Russel, A. (2022). Dynamic Calibration of GPS Effective Isotropic Radiated Power for GNSS-Reflectometry Earth Remote Sensing. *IEEE Transactions on Geoscience and Remote Sensing*, *60*, 1–12. https://doi.org/10.1109/TGRS.2021.3070238